



LLMind: Bio-inspired Training-free Adaptive Visual Representations for Vision-Language Models

Soumyaratna Debnath Bui Duc Manh Zinan Liu Lin Wang[†]
Nanyang Technological University, Singapore

soumyara004@e.ntu.edu.sg ducmanh.bui@ntu.edu.sg zinan001@e.ntu.edu.sg linwang@ntu.edu.sg

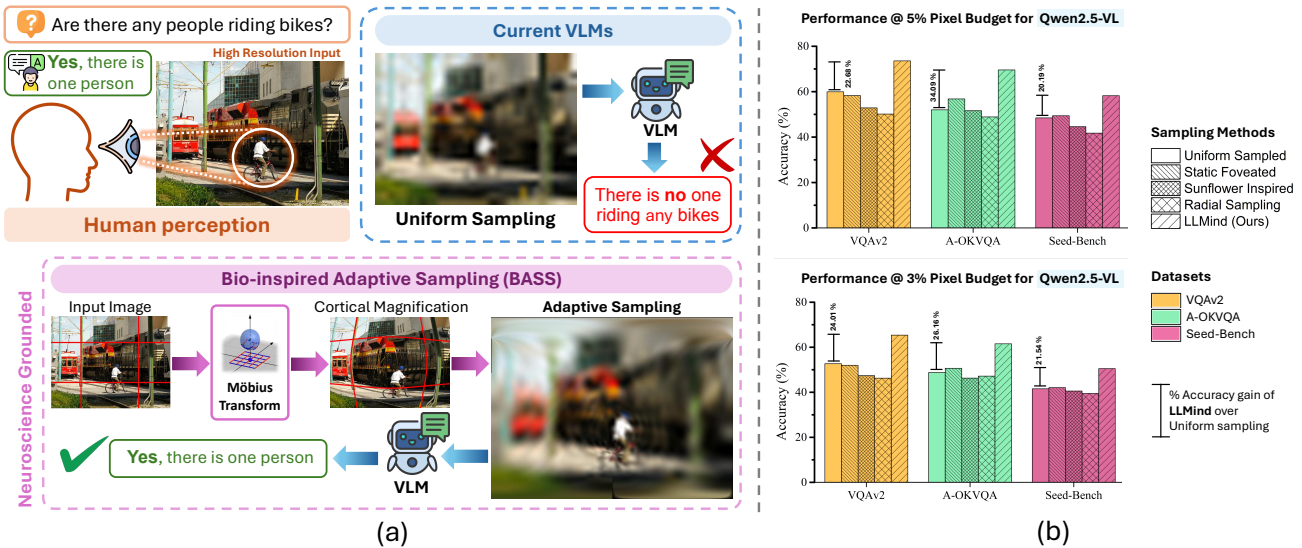


Figure 1. (a) Illustration of the underlying principle of our Bio-inspired Adaptive Sampling Strategy (BASS). (b) Performance comparison at 5% and 3% pixel budgets using Qwen2.5-VL [5] across datasets. Project page: <https://empaqlab.github.io/LLMind-CVPR-2026/>

Abstract

Vision-Language Models (VLMs) typically assume a uniform spatial fidelity across the entire field of view of visual inputs, dedicating equal precision to even the uninformative regions. By contrast, human vision is neither uniform nor static. It is adaptive, selective, and resource-efficient. In light of this, we present the **first** systematic analysis of bio-inspired visual representation methods, providing insights for more efficient and adaptive VLMs. We propose **LLMind (Looking Like the Mind)**, a novel **training-free** framework that mimics foveated encoding and cortical magnification in human vision to achieve **adaptive, efficient** representations for VLMs under tight pixel budgets. Our key idea is to explore a **Bio-inspired Adaptive Sampling Strategy (BASS)**. This empowers us to design a **Möbius-parameterized** module that **performs non-uniform sampling while preserving global scene structure**. On top of BASS, we introduce **closed-loop semantic feedback (CSF)** via test-time adapta-

[†]Corresponding author.

tion to align the perceptual saliency with the textual information from the frozen VLM. We evaluate LLMind against uniform and other sampling baselines across diverse scene-level and region-guided visual question answering (VQA) benchmarks. The results show that ours achieves dramatic gains, with average improvements by **+20%** on VQAv2, **+38%** on Seed-Bench, and **+37%** on A-OKVQA compared to uniform sampling under tight pixel budgets. More surprisingly, results reveal that LLMind can retain up to **82%**, **92%** and **97%** of the full-resolution performance with only **1%**, **3%** and **5%** of the pixels, respectively. Moreover, LLMind is **lightweight, plug-and-play, and compatible** with existing VLMs without requiring architectural changes.

1. Introduction

Vision-Language Models (VLMs) have recently demonstrated impressive progress in multimodal reasoning and visual question answering (VQA) [3, 10, 32, 46]. By jointly encoding visual and textual cues, these models can infer semantic correspondences and generate contextually coherent

responses. However, despite these advances, existing models still operate under an assumption: *perception requires uniform access to every pixel of an image* [42, 48]. For instance, typical VLMs, e.g., Qwen [50] or LLaVA [31] based on attention mechanisms do not employ attention to modulate the spatial sampling of visual inputs [27]. Attention in transformers redistributes representational emphasis across features, but the underlying image is still uniformly sampled at fixed resolution. Consequently, VLMs allocate equal computational resources to semantically irrelevant background regions and critical foreground details alike [8, 23]. While computationally tractable at small scales, these models become inefficient as image resolution increases, forcing models to uniformly downsample and, consequently, discard critical details from all regions of the image. Although dynamic tokenization [7, 39] has recently been introduced to address such issues, it still requires full-resolution input, which limits its suitability for edge systems.

From a neuroscience perspective, uniform downsampling does not reflect how biological vision allocates computational resources [42, 48]. Instead, the human visual system employs a hierarchical, attention-driven foveation strategy: the fovea provides high-acuity detail in a small attended region, while the peripheral retina conveys coarse, context-rich information that guides subsequent gaze shifts and processing [44] (Fig. 1 (a)). Through rapid saccadic movements, the visual system dynamically repositions this high-resolution window, sampling the scene adaptively based on task demands [25, 29]. This mechanism reflects the principle of **cortical magnification**, where perceptually salient regions occupy disproportionately large representational space in the visual cortex [14]. Perception, therefore, is not a static snapshot but an active optimization process that maximizes information gain while minimizing computational expenditure [16].

Inspired by the foveated encoding and cortical magnification in human vision, an interesting question arises: *Can biologically inspired sampling strategies enable VLMs to achieve higher reasoning efficiency and accuracy than conventional uniform sampling under limited pixel budgets?* To answer this, we present the first comprehensive analysis of the visual representation strategies in VLMs, evaluating their effectiveness against uniform sampling across multiple VQA benchmarks. Building on this, we propose **LLMind**, a novel adaptive sampling framework that emulates the human visual system for the visual stimuli.¹ Our core idea is to explore a Bio-inspired Adaptive Sampling Strategy (**BASS**) (Sec. 3.1). BASS serves as a computational analogue of cortical magnification, wherein the foveal region occupies a disproportionately large cortical representation [11]. To make it possible, we use Möbius transformation [4, 37], a mathematical tool that is parame-

¹Here, visual stimuli correspond to the input image of VLMs.

terized to simulate cortical magnification. As a conformal mapping on the spherical plane, Möbius transformations perform smooth mappings of the image space (i.e. rotation, translation, scaling, inversion) while preserving local geometry. As such, we can dynamically remap the spatial domain of an image, magnifying task-relevant regions with higher sampling density while compressing peripheral areas.

We optimize the BASS parameters in a training-free loop using a perceptual loss, guided by the semantic output of the frozen VLM. Since the frozen VLM model is non-differentiable, we then introduce closed-loop semantic feedback (**CSF**) via test-time adaptation using Simultaneous Perturbation Stochastic Approximation [43] to estimate gradients directly from input-output interactions (Sec. 3.2). Unlike prior training-free methods that require access to internal model parameters or gradients of open (*white-box*) VLM [49], our gradient-free CSF strategy can also seamlessly integrate with proprietary (*black-box*) APIs, requiring no architectural modifications or parameter access.

We extensively evaluate LLMind against uniform and other sampling baselines across diverse benchmark datasets, considering two complementary VQA paradigms: *Scene-level VQA* for holistic reasoning and *Region-guided VQA* for localized understanding. LLMind improves the average performance² by **+20%** on VQAv2 [21], **+38%** on *Seed-Bench* [30], and **+37%** on *A-OKVQA* [41] compared to uniform sampling under the same pixel budget for scene-level VQA tasks. For region-guided VQA, LLMind achieves an average gain of **35%** over uniform sampling, even surpassing the full-resolution accuracy while using only 1% of the pixels (See Sec. 4.3).

To summarise, the major contributions of this paper are:

- Inspired by neuroscience-grounded knowledge, we identify a fundamental problem in VLMs and conduct the first comprehensive analysis of the visual representation strategies in VLMs.
- We propose BASS that dynamically reallocates pixel budget to perceptually and semantically salient regions as a computational analogue of human vision (Sec. 3.1).
- We introduce the CSF mechanism that aligns visual perception with task-driven reasoning in a training-free, test-time optimization compatible with both white-box and black-box VLMs (Sec. 3.2).
- We validate our method on standard VQA benchmarks, demonstrating consistent improvements in reasoning accuracy under constrained pixel budgets for both scene-level and region-guided settings (Sec. 4.3).

2. Related Works

Multi-Resolution and Non-Uniform Visual Sampling.

Early studies modeled the human visual system to understand the functional limits of peripheral vision [6, 15],

²Average across 1%, 3% and 5% pixel budgets.

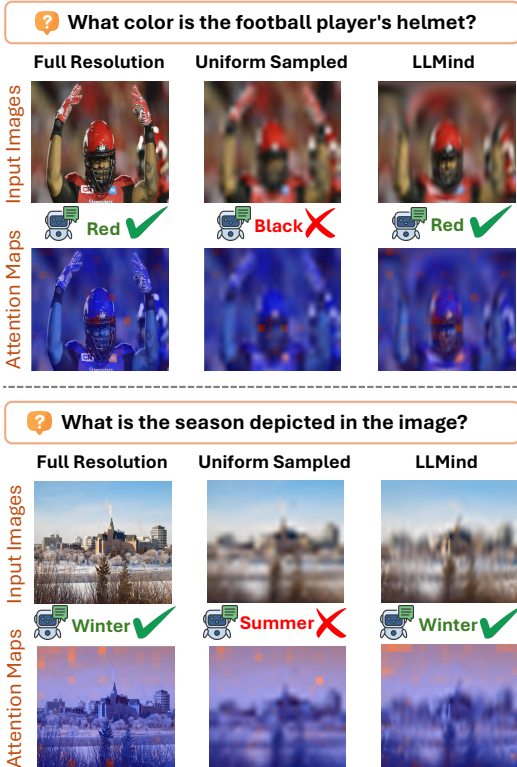


Figure 2. **Qualitative comparison with Qwen2.5-VL on Seed-Bench at 5% pixel budget.** LLMind adaptively allocates resolution to semantically important regions, preserving visual evidence critical for answering the question. *Zoom in for a better view.*

but did not translate these insights to AI-based systems. Later research extended this direction by applying foveated texture-based input representations to deep networks, showing that peripheral texture encoding enhances generalization, high-frequency sensitivity, and robustness to occlusion [12, 24]. A neuro-computational model further suggested that the advantage of peripheral over central vision arises from the intrinsic utility of peripheral features, which generate a broader representational spreading transform [45]; however, this work was limited to scene classification. Some works have even explored biologically inspired retinal sampling to mimic foveal vision and reduce visual redundancy for prosthetic or neuromorphic applications [40], but these methods remain hardware-bounded, and limited to low-level sensory encoding. Recent studies have examined how multi-resolution processing contributes to robustness and efficiency in vision models [1, 17]. In an effort to exploit spatially adaptive representations, several works have explored non-uniform sampling, particularly foveated schemes that densely sample regions near a fixation point while sparsifying the periphery [2, 34, 38]. However, these approaches often introduced new task-specific architectures rather than utilizing existing pretrained ones.

Foveation in Modern Neural Architectures. Building

upon the foundations of non-uniform visual sampling, recent works have integrated foveation principles into modern neural architectures. PerViT [36] modeled peripheral vision by injecting biologically inspired inductive biases into Transformer self-attention, while Killick *et al.* [28] introduced an end-to-end differentiable foveated vision model using graph convolution and sunflower-patterned sampling. Costa *et al.* [9] further explored cortical magnification by incorporating a retinal sampling layer that reproduced foveal magnification and radial bias through ganglion-cell-based resampling. However, these approaches remain task-specific, training-dependent, and limited to image classification tasks. Thus, most prior works have focused on simpler single-modality tasks and has limited insight into how biologically inspired sampling can enhance higher-level reasoning in VLMs.

Recently, two works by Gizdov *et al.* [19, 20] demonstrated that variable-resolution sampling improves VQA and detection accuracy in existing Large multimodal models (LMM) under tight pixel budgets. However, their sampling scheme remains static, single-fixation, and does not account for salient or semantic features. In contrast, our framework performs dynamic, inference-time adaptive sampling that accounts for both salient and semantic features under strict pixel constraints, thereby improving performance over Gizdov *et al.* [19, 20].

Training-Free Optimization for Multimodal Adaptation. Recent works have explored training-free optimization in multimodal systems through visual prompt manipulation [26, 49]. ControlMLLM [49], for example, optimized latent variables over attention maps at test time to guide focus toward region-of-interest cues. Our framework draws inspiration from this paradigm but differs fundamentally: rather than optimizing over attention maps, we optimize the sampling transformation itself, thereby modulating the visual input before encoding. Moreover, while most training-free frameworks, including ControlMLLM, still require access to internal attention maps or gradients, thus operating in a white-box setting. Our method is entirely black-box compatible, functioning seamlessly with closed-source VLMs without any internal model access.

3. Methodology

Overview: An overview of the proposed framework is illustrated in Fig. 3. The core of our design is a **Bio-inspired Adaptive Sampling Strategy (BASS)** that serves as a front-end sampling module. Based on a Möbius transformation, this generator produces a sampling grid that allocates resolution dynamically, mimicking the foveated structure of the human eye. The transformation parameters are optimized at inference time through a perceptual loss and CSF, analogous to the saccadic eye movement that continuously refines human visual focus. Formally, given an image

$I \in \mathcal{R}^{H \times W \times 3}$ and a set of questions q , the framework produces an adaptively sampled image \hat{I} that maximizes reasoning accuracy under a constrained pixel budget B .

$$\hat{I} = \arg \max_{\mathbb{E}_\theta(I)} \mathcal{F}(\hat{I}, q, \theta_f), \quad (1)$$

where \mathbb{E}_θ denotes the BASS module, parameterized by Möbius transformation coefficients θ and \mathcal{F} denotes the frozen VLM’s response quality.

3.1. Bio-inspired Adaptive Sampling Strategy

Insight. Inspired by the non-uniform spatial acuity of the human visual system, we design a Möbius transformation-based Bio-inspired Adaptive Sampling Strategy (BASS) (See Fig. 4). Möbius transformation provides a continuous, conformal mapping of the image plane. It bends the image space so that the cognitive region is magnified while the surrounding areas are smoothly compressed.

Forward and Inverse Möbius Warp. We apply a Möbius transformation to the input images via stereographic projection. Given an input image I , each pixel corresponds to a spherical direction $\mathbf{s} \in S^2$. We first map \mathbf{s} to the complex plane using north-pole stereographic projection $\Sigma : S^2 \rightarrow \mathbb{C}$, yielding $w = \Sigma(\mathbf{s})$. The Möbius transformation used in our model is parameterized by real scalars a, b, c, d (normalized to avoid degenerate matrices), and is applied in the complex domain, and the transformed complex value z is defined as:

$$z = \frac{aw + b}{cw + d} \quad (2)$$

z is then mapped back to a point on the sphere via the inverse stereographic projection Σ^{-1} , and finally projected back into image coordinates using the standard mapping Π . Therefore, the overall forward warp $\mathcal{M}(I)$ is:

$$\mathcal{M}(I)[u, v] = I^* \left(\Pi \left(\Sigma^{-1} \left(\frac{d \Sigma(\mathbf{s}(u, v)) - b}{-c \Sigma(\mathbf{s}(u, v)) + a} \right) \right) \right) \quad (3)$$

where I^* denotes bilinear sampling and $\mathbf{s}(u, v)$ converts the image pixel (u, v) to its corresponding spherical direction. The inverse warp uses the inverse Möbius z^{-1} , defined as:

$$z^{-1} = \frac{dw - b}{-cw + a}, \quad (4)$$

resulting in the inverse transformation $\mathcal{M}^{-1}(I)$:

$$\mathcal{M}^{-1}(I)[u, v] = I^* \left(\Pi \left(\Sigma^{-1} \left(\frac{a \Sigma(\mathbf{s}(u, v)) + b}{c \Sigma(\mathbf{s}(u, v)) + d} \right) \right) \right) \quad (5)$$

Learning the Möbius Parameters. In our implementation, a lightweight Multilayer Perceptron (MLP) predicts the Möbius parameters, which we represent as a real-valued vector $\theta \in \mathcal{R}^4$, corresponding to the real part of the coefficients of the Möbius transformation. To incorporate this into an adaptive image sampling framework, we formulate the Sampling Strategy \mathbb{E}_θ as a differentiable mapping:

$$\hat{I} = \mathbb{E}_\theta(I) = \mathcal{M}_\theta^{-1}(\mathcal{I}(\mathcal{S}_B(\mathcal{M}_\theta(I)))) \quad (6)$$

where $\mathcal{M}_\theta(\cdot)$ and $\mathcal{M}_\theta^{-1}(\cdot)$ denote the forward and inverse Möbius transforms parameterized by θ (Eq. 3 and Eq. 5 respectively), $\mathcal{S}_B(\cdot)$ performs uniform sampling at a controlled pixel budget B , and $\mathcal{I}(\cdot)$ denotes the interpolation operator (e.g. bilinear interpolation) to restore the image to the original resolution.

3.2. Closed-Loop Semantic Feedback

Insight. We introduce the CSF module to adapt the sampling based on semantics cues via test-time adaptation of the BASS parameters, ensuring that the visual detail is allocated to regions most relevant to the task.

Perceptual Loss. Our perceptual loss is designed to achieve two primary objectives: maintaining global perceptual fidelity and accentuating semantically salient structures. To this end, we define a composite loss function:

$$\mathcal{L}_{img} = \alpha \cdot \mathcal{L}_{VSI} + \beta \cdot \mathcal{L}_{DISTS} + \gamma \cdot \mathcal{L}_{MSE} \quad (7)$$

where α, β and γ are weighting coefficients. \mathcal{L}_{img} balances semantic saliency, structural integrity, and optimization stability. It combines a **Visual Saliency-Induced Index (VSI)** [52] term to prioritize human-attentive regions, a **Deep Image Structure and Texture Similarity (DISTS)** [13] metric to enforce perceptual alignment in feature space, and a **Mean Squared Error (MSE)** regularizer to ensure pixel-level smoothness and stabilize training.

Semantic Loss. While the perceptual loss \mathcal{L}_{img} preserves visual quality, the challenge is how to improve semantic reasoning accuracy for the given question q . We therefore integrate textual feedback from the frozen VLM by comparing predicted answers with ground-truth responses. Given the model’s predicted answer y_{pred} and reference answer y_{gt} , we compute the text loss as:

$$\mathcal{L}_{text} = 1 - \cos(E(y_{pred}), E(y_{gt})) \quad (8)$$

where $E(\cdot)$ denotes normalized embeddings obtained from a Sentence Transformer (MiniLM [47]). This formulation captures semantic similarity rather than exact string matching, making it robust to paraphrasing. Since the VLM operates as a black box, gradients from \mathcal{L}_{text} cannot be directly propagated through the model. To address this, we employ **Simultaneous Perturbation Stochastic Approximation (SPSA)** to estimate the gradient. Let $\theta \in \mathbb{R}^4$ represent the Möbius transformation parameters. The gradient estimate is computed as:

$$\nabla_\theta \mathcal{L}_{text} \approx \frac{\mathcal{L}_{text}(\theta + \delta \Delta) - \mathcal{L}_{text}(\theta - \delta \Delta)}{2\delta} \quad (9)$$

where $\delta > 0$ is a small perturbation size, and $\Delta \in \mathbb{R}^4$ is a random perturbation vector with components sampled from a symmetric Bernoulli distribution, i.e., $\Delta_i \sim \{\pm 1\}$ with equal probability.

Furthermore, to improve training efficiency, we employ an adaptive question selection strategy that focuses on challenging examples. Let $\mathcal{Q} = \{q_1, \dots, q_N\}$ be the set of

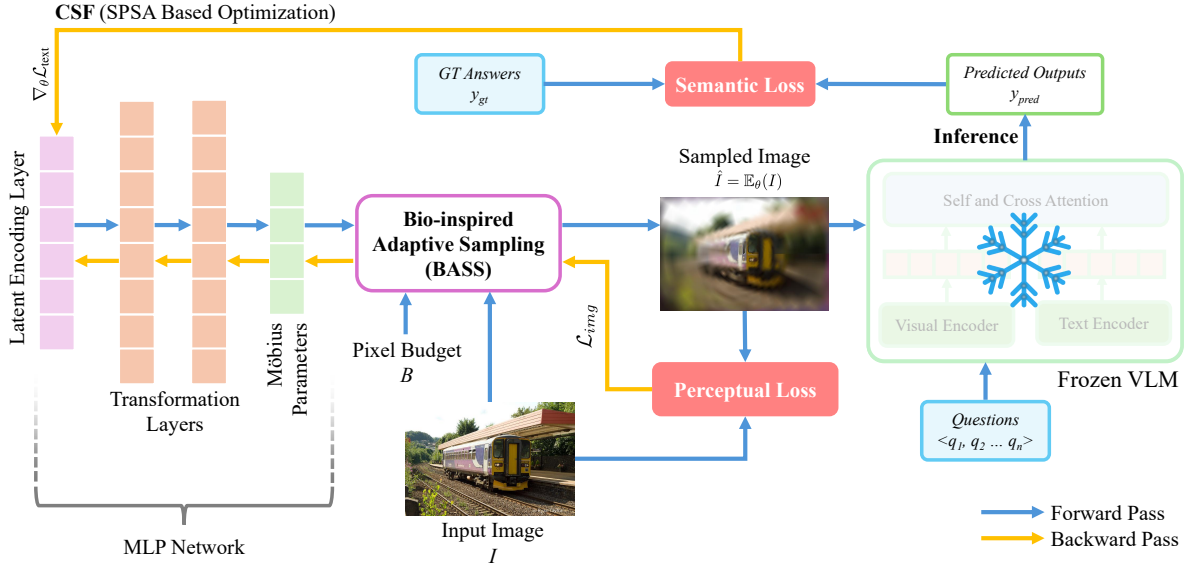


Figure 3. **Overview of the proposed framework.** Given the input image I , the MLP network predicts the Möbius transformation coefficients, which are used by BASS (Sec. 3.1) to produce the sampled image \hat{I} . The Perceptual loss \mathcal{L}_{img} (Eq. 7) between I and \hat{I} flows through the network to optimize the MLP parameters. In parallel, a frozen VLM processes a set of questions q to generate predicted answers y_{pred} . These are compared with the ground-truth answers y_{gt} to obtain the Semantic loss $\mathcal{L}_{\text{text}}$ (Eq. 8) for further guiding the optimization of the MLP parameters using SPSA (Eq. 9).

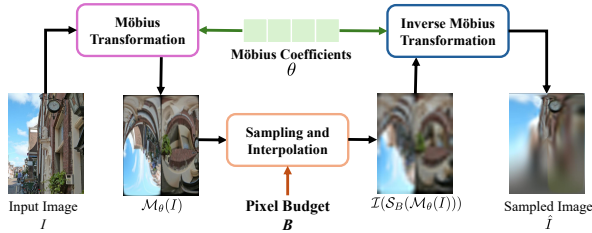


Figure 4. **Illustration of the Bio-inspired Adaptive Sampling Strategy (BASS).** Given an input image I , the MLP predicts Möbius parameters θ to warp the image toward salient regions (Eq. 3). The warped image is uniformly sampled under pixel budget B through $\mathcal{S}_B(\cdot)$, and then reconstructed to its original resolution via an interpolation operator $\mathcal{I}(\cdot)$. Finally, the inverse transformation (Eq. 5) restores the global spatial structure, yielding the adaptively sampled image \hat{I} .

all questions and $w_i^{(t)}$ be the weight associated with question q_i at optimization step t . We initialize weights uniformly: $w_i^{(0)} = 1/N$. After each evaluation, weights are updated exponentially based on performance: $w_i^{(t+1)} = w_i^{(t)} \cdot \exp\left(\eta \cdot \frac{\mathbb{I}[q_i \text{ is wrong}]}{N}\right)$, where $\eta > 0$ is a learning rate and $\mathbb{I}[\cdot]$ is the indicator function. Questions for SPSA gradient estimation are then sampled proportionally to their current weights $P(\text{select } q_i) = \frac{w_i}{\sum_{j=1}^N w_j}$. We formulate the final optimization objective as a weighted combination of the perceptual and semantic losses. Let \mathcal{L}_{img} be the perceptual loss and $\beta > 0$ a balancing coefficient. The combined up-

date direction is:

$$g_{\text{total}} = \nabla_{\theta} \mathcal{L}_{\text{img}} + \beta \cdot \frac{\|\nabla_{\theta} \mathcal{L}_{\text{img}}\|}{\|\nabla_{\theta} \mathcal{L}_{\text{text}}\|} \nabla_{\theta} \mathcal{L}_{\text{text}} \quad (10)$$

where gradient norms are computed for numerical stability. This enables gradient-free optimization while maintaining focus on semantically challenging cases, even when the VLM’s internal gradients are inaccessible.

4. Experiments and Evaluation

4.1. Settings and Implementation Details

Evaluation Details. We evaluate the LLMind across two complementary VQA paradigms that jointly examine its capability for holistic scene understanding as well as region-guided reasoning. For all experiments, we restrict our study to *lightweight VLMs* ($< 4\text{B}$ parameters) to emphasize the framework’s adaptability in low-resource scenarios. This choice reflects a *practical motivation*: recent works show that small-scale models, with efficient design choices and sampling mechanisms, can approach their larger counterparts [18, 35]. Our experiments, therefore, highlight how the proposed method enhances reasoning ability without relying on massive model capacity.

(1) Scene-level VQA. We evaluate the model’s capability for global reasoning over the entire visual scene. The questions demand comprehension of semantic relationships, contextual attributes, and high-level visual concepts present across the image. For example, queries such as “What best describes the pool of water?” or “How many

Table 1. **Quantitative comparison of bio-inspired and uniform sampling strategies on scene-level VQA benchmarks under tight-budget constraints (1%, 3%, 5%).** We report full-resolution accuracy, sampled accuracy at each budget, accuracy gain over uniform sampling, and accuracy retained relative to the full-resolution baseline.

Dataset	Model	Accuracy (%) Full Res.	Sampling Method	Accuracy Sampled (%)			Δ Accuracy Gain (%) over Uniform Sample			Accuracy Retained (% of Full Res.)		
				1%	3%	5%	1%	3%	5%	1%	3%	5%
VQAv2	Qwen2.5-VL	86.96	Uniform Sampling	47.31	52.71	59.94	–	–	–	54.40	60.61	68.92
			Static Foveated	46.18	51.96	58.30	-2.38	-1.42	-2.73	53.10	59.75	67.04
			Sunflower Inspired	43.77	47.41	52.85	-7.48	-10.05	-11.82	50.33	54.51	60.77
			Radial Sampling	44.79	46.25	50.12	-5.32	-12.25	-16.38	51.50	53.18	57.63
			LLMind (Ours)	55.05	65.37	73.54	+16.36	+24.01	+22.68	63.31	75.17	84.56
	SmolVLM	80.01	Uniform Sampling	46.38	53.28	59.06	–	–	–	57.96	66.59	73.81
			Static Foveated	44.24	51.64	58.43	-4.61	-3.07	-1.06	55.29	64.54	73.02
			Sunflower Inspired	46.45	50.55	56.38	+0.15	-5.12	-4.53	58.05	63.17	70.46
			Radial Sampling	42.99	47.07	50.92	-7.30	-11.65	-13.78	53.73	58.83	63.64
			LLMind (Ours)	58.88	70.40	76.46	+26.95	+32.13	+29.46	73.59	87.98	95.56
	LLaVA-OneVision	73.34	Uniform Sampling	40.98	49.15	57.60	–	–	–	55.87	67.01	78.53
			Static Foveated	42.27	42.88	45.37	+3.14	-12.75	-21.23	57.63	58.46	61.86
Sunflower Inspired			42.29	46.02	50.51	+3.19	-6.36	-12.30	57.66	62.74	68.87	
Radial Sampling			40.10	42.40	45.25	-2.14	-13.73	-21.44	54.67	57.81	61.69	
LLMind (Ours)			47.00	54.49	62.38	+14.69	+10.86	+8.29	64.08	74.29	85.05	
A-OKVQA	Qwen2.5-VL	85.67	Uniform Sampling	44.31	48.77	52.01	–	–	–	51.72	56.93	60.71
			Static Foveated	45.58	50.65	56.78	+2.87	+3.85	+9.17	53.20	59.12	66.28
			Sunflower Inspired	43.23	46.28	51.61	-2.44	-5.11	-0.77	50.46	54.02	60.24
			Radial Sampling	45.58	47.16	48.90	+2.87	-3.30	-5.98	53.20	55.05	57.08
			LLMind (Ours)	51.18	61.53	69.74	+15.50	+26.16	+34.09	59.74	71.82	81.41
	SmolVLM	78.60	Uniform Sampling	39.78	45.06	48.73	–	–	–	50.61	57.33	62.00
			Static Foveated	42.09	46.98	51.44	+5.81	+4.26	+5.56	53.55	59.77	65.45
			Sunflower Inspired	44.27	46.20	48.64	+11.29	+2.53	-0.18	56.32	58.78	61.88
			Radial Sampling	41.48	43.58	47.33	+4.27	-3.28	-2.87	52.77	55.45	60.22
			LLMind (Ours)	64.81	72.63	76.81	+62.92	+61.19	+57.62	82.46	92.40	97.72
	LLaVA-OneVision	60.26	Uniform Sampling	34.80	35.71	42.33	–	–	–	57.75	59.26	70.25
			Static Foveated	34.23	35.28	37.27	-1.64	-1.20	-11.95	56.80	58.55	61.85
Sunflower Inspired			27.68	30.91	36.24	-20.46	-13.44	-14.39	45.93	51.29	60.14	
Radial Sampling			28.29	28.03	29.78	-18.71	-21.51	-29.65	46.95	46.52	49.42	
LLMind (Ours)			43.01	46.09	53.18	+23.59	+29.07	+25.63	71.37	76.49	88.25	
Seed Bench	Qwen2.5-VL	71.25	Uniform Sampling	35.53	41.55	48.45	–	–	–	49.87	58.32	68.00
			Static Foveated	34.75	42.05	49.4	-2.20	+1.20	+1.96	48.77	59.02	69.33
			Sunflower Inspired	36.70	40.55	44.6	+3.29	-2.41	-7.95	51.51	56.91	62.60
			Radial Sampling	35.20	39.45	41.75	-0.93	-5.05	-13.83	49.40	55.37	58.60
			LLMind (Ours)	40.28	50.50	58.23	+13.37	+21.54	+20.19	56.53	70.88	81.73
	SmolVLM	51.6	Uniform Sampling	21.81	26.38	29.19	–	–	–	42.27	51.12	56.57
			Static Foveated	30.20	36.85	42.65	+38.47	+39.69	+46.11	58.53	71.41	82.66
			Sunflower Inspired	33.60	34.95	37.85	+54.06	+32.49	+29.67	65.12	67.73	73.35
			Radial Sampling	30.80	33.15	36.05	+41.22	+25.66	+23.50	59.69	64.24	69.86
			LLMind (Ours)	37.42	43.44	45.97	+71.57	+64.67	+57.49	72.52	84.19	89.09
	LLaVA-OneVision	37.75	Uniform Sampling	18.65	21.60	24.35	–	–	–	49.40	57.22	64.50
			Static Foveated	24.85	25.55	25.60	+33.24	+18.29	+5.13	65.83	67.68	67.81
Sunflower Inspired			21.40	23.90	25.15	+14.75	+10.65	+3.29	56.69	63.31	66.62	
Radial Sampling			22.90	21.70	22.55	+22.79	+0.46	-7.39	60.66	57.48	59.74	
LLMind (Ours)			26.05	27.85	30.40	+39.68	+28.94	+24.85	69.01	73.77	80.53	

people are visible in the image?” require a holistic understanding spanning the full spatial extent. We conduct experiments on 5000+ question-answer pairs from VQAv2 and 2000+ pairs from Seed-Bench to evaluate general scene-level reasoning capabilities for LLMind. Additionally, we evaluate LLMind on A-OKVQA dataset, which requires integrating external, world-based knowledge for comprehensive visual understanding.

(2) **Region-guided VQA.** We evaluate the model’s localized reasoning by using explicit region prompts to direct

the model’s focus toward relevant spatial areas. Each question is associated with a bounding region that defines a *cognitive window*. The questions require interpreting spatial cues to perform region-specific classification (RSC) within the defined cognitive window. For example, “Is the object (location) a (class A) or a (class B)?” or “Can you provide a description of the region (location)?”. We adopt data configuration as ControlMLLM [49] for this setting, following the Ferret [51] setup to construct 1400+ region-guided questions from the LVIS [22] validation split.

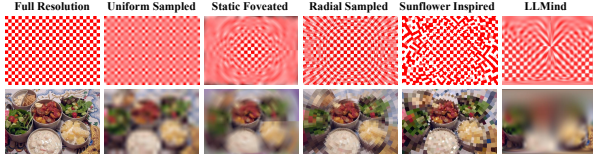


Figure 5. Illustration of the compared sampling methods under 10% pixel budget. *Zoom in for a better view.*

Implementation Details. All experiments were conducted on a system equipped with $4 \times$ NVIDIA GeForce RTX 5090 GPUs (32 GB VRAM each). For each image, we perform an inference-time optimization for a fixed number of iterations t . Within this process, the SPSA update step is applied every $t/5$ iterations in equal intervals. Unless otherwise specified, all images are processed at their original resolution without resizing.

We adopt the concept of **information-matched images** proposed by Gizdov *et al.* [20], which provides a principled way to compare sampling strategies under identical pixel budgets. Specifically, two sampling maps are constructed such that they contain the same number of sampled pixels, differing only in how those samples are spatially distributed. This ensures that any observed performance differences arise purely from the sampling distribution rather than from differences in information content.

The computational overhead for LLMind is marginal and bounded by t , with latency of ~ 0.011 s/iter w/o SPSA and ~ 4.75 s/iter with SPSA (reducible via optimizations [49]).

4.2. Baseline Methods

Fig. 5 illustrates the sampling baselines evaluated in our study alongside LLMind. Each method allocates the same total information budget but differs in how resolution is spatially distributed across the visual field. After sampling, all representations are upsampled via interpolation to the original input resolution, ensuring that any performance differences arise purely from the sampling distribution rather than from differences in input size.

(1) **Uniform Sampling.** We include a uniform sampling condition as a baseline, where the same total pixel budget is spread evenly across the entire image.

(2) **Static Foveated.** We implement the static-foveated baseline following the formulation of Gizdov *et al.* [19, 20], using log-polar sampling to generate variable-resolution inputs. Consistent with the original setting, the fixation point is fixed at the image center throughout all experiments.

(3) **Sunflower Inspired.** We adopt a biologically inspired sampling layout following the sunflower phyllotaxis model proposed by Killick *et al.* [28]. Unlike the original work, we employ this sampling formulation purely as a static input transformation without the graph-convolutional processing. Following the static foveate setting, the fixation is fixed at the image center.

(4) **Radial Sampling.** We implement a static radial sam-

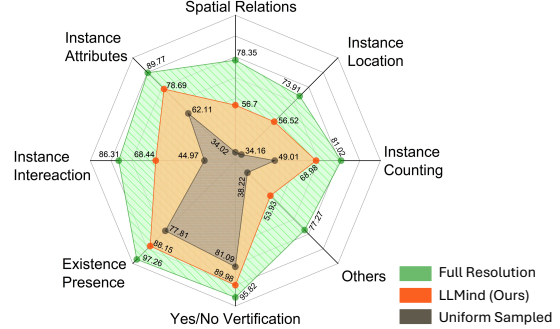


Figure 6. Category-wise performance on A-OKVQA at a 5% pixel budget with Qwen2.5-VL (4B). *Zoom in for a better view.*

pling scheme inspired by the retinal model of Robert-Inacio *et al.* [40]. The fixation is fixed at the image center, and the foveal region is preserved at full resolution, while maintaining the overall information-matched constraint so that the total number of sampled pixels remains consistent.

4.3. Results and Discussion

Our experimental results are structured around the following research questions (RQs), which guide our evaluation:

RQ-1: Does LLMind improve scene-level VQA accuracy across diverse benchmarks by selectively allocating pixels to semantically informative regions?

RQ-2: Can LLMind enhance region-guided VQA accuracy by reducing background distraction and improving evidence grounding?

RQ-3: What is the impact of the CSF module on sampling quality across different pixel budgets, and how essential is it for semantic alignment?

4.3.1. Comparison on Scene-level VQA.

Table 1 presents the quantitative results on VQAv2, Seed-Bench, and A-OKVQA under strict pixel budgets (1–5%), evaluated across Qwen2.5-VL [5] (4B), SmolVLM [35] (2B), and LLaVA-OneVision [31] (0.9B).

[A-1] LLMind consistently outperforms all competing sampling strategies under strict pixel budgets. It retains more than **55%** of the full-resolution accuracy at only 1% pixels, over **70%** at 3%, and above **80%** at 5% across all benchmarks. At peak efficiency, LLMind preserves up to **82%**, **92%**, and **97%** of the full-resolution performance at the 1%, 3%, and 5% budgets.

Fig. 2 provides qualitative comparisons on Seed-Bench for Qwen2.5-VL, including attention visualizations. LLMind’s attention closely aligns with the full-resolution model, consistently focusing on the evidence-relevant regions, whereas uniform sampling produces diffuse and often misplaced attention. Moreover, the question-category-wise analysis (Fig. 6) reveals that LLMind improves performance across all major reasoning categories, indicating broad gains that extend beyond any specific task type.

Table 2. Performance comparison of various sampling methods for a single RSC-based VQA task on the LVIS dataset.

Model	Accuracy (%) Full Res.	Sampling Method	Accuracy Sampled (%)			
			1%	3%	5%	10%
Qwen3-VL	50.60	Uniform Sampling	44.80	45.63	50.40	51.60
		Static Foveated	46.10	48.50	49.40	50.40
		Sunflower Inspired	47.60	47.50	49.70	49.50
		Radial Sampling	45.30	46.70	48.10	48.20
		LLMind (Ours)	54.60	62.90	71.40	77.50
DeepSeek-VL	46.10	Uniform Sampling	43.50	43.90	44.10	47.80
		Static Foveated	44.50	45.00	44.80	45.20
		Sunflower Inspired	43.90	44.40	44.60	44.50
		Radial Sampling	44.30	44.30	45.20	44.43
		LLMind (Ours)	53.20	59.20	62.20	66.80

4.3.2. Comparison on Region-guided VQA.

Table 2 and Table 3 present results for single- and multi-region guided VQA on the LVIS dataset, where each question specifies a cognitive window. We evaluate Qwen3-VL [50] (2B) and DeepSeek-VL [33] (2B) in this setting, which requires performing region-specific classification (RSC) through VQA within the cognitive window.

[A-2] LLMind consistently surpasses all baselines under both single and multi-region guided VQA. With only 3% pixels, LLMind even **outperforms the full-resolution input**, indicating that removing irrelevant visual content can reduce distraction and improve reasoning fidelity.

The targeted visual allocation in LLMind explains its ability to surpass full-resolution inputs in region-guided tasks. Small VLMs such as Qwen3 (2B) and DeepSeek-VL (2B) achieve below 60% accuracy at full resolution, indicating limited robustness in this setting. By revealing only evidence-relevant regions and suppressing background clutter, LLMind reduces the influence of background clutter and scene-level priors that often lead to hallucinations. As a result, the model makes decisions that are more closely grounded in the specified regions, leading to more reliable and accurate reasoning.

4.3.3. Ablation and Analysis

We conduct an ablation study on the A-OKVQA dataset using Qwen2.5-VL to analyze the roles of pixel budget and the CSF module (Fig. 7).

[A-3] Without CSF, LLMind relies only on perceptual similarity, yielding gains over Uniform Sampling at low pixel budgets but diminishing at higher budgets where perceptual cues fail to highlight semantic regions. With CSF, performance improves consistently across all pixel budgets, showing that semantic feedback is essential for guiding sampling toward task-relevant evidence.

With CSF, LLMind achieves even stronger gains: at only 20% of the sampled pixels, it **surpasses the full-resolution accuracy**, indicating that VLMs do not inherently require the entire image to perform well. When sampling is guided

Table 3. Performance comparison of various sampling methods for multiple RSC-based VQA tasks on the LVIS dataset.

Model	Accuracy (%) Full Res.	Sampling Method	Accuracy Sampled (%)			
			1%	3%	5%	10%
Qwen3-VL	60.20	Uniform Sampling	50.90	53.49	55.30	56.85
		Static Foveated	50.38	52.19	53.74	56.58
		Sunflower Inspired	51.16	53.22	55.29	56.07
		Radial Sampling	48.83	50.64	51.42	56.07
		LLMind (Ours)	60.21	66.41	72.61	77.26
DeepSeek-VL	51.93	Uniform Sampling	43.15	45.22	47.29	50.39
		Static Foveated	44.96	48.57	52.45	51.42
		Sunflower Inspired	42.63	47.02	48.57	49.87
		Radial Sampling	43.15	45.21	45.73	50.38
		LLMind (Ours)	50.90	60.47	65.12	65.63

adaptively toward semantically relevant regions, the model can match and even exceed the performance obtained from full-resolution inputs. We also observe **diminishing returns** beyond the 20% pixel budget. The accuracy gradually converges toward the full-resolution performance as the pixel budget increases.

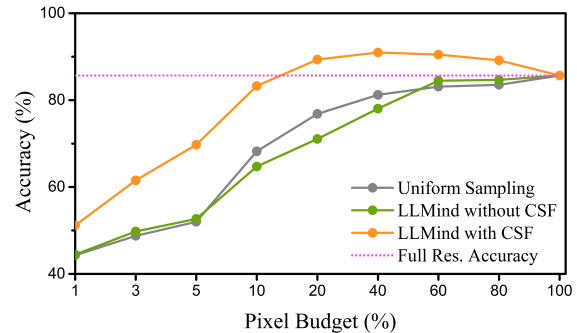


Figure 7. Ablation study on A-OKVQA dataset with Qwen2.5-VL (4B) illustrating the impact of pixel budget and the CSF module on LLMind’s performance. *Zoom in for a better view.*

5. Conclusion and Future Work

In this work, we investigated the role of biologically inspired sampling in enhancing visual reasoning under constrained pixel budgets. We introduced **LLMind**, a training-free adaptive sampling strategy inspired by cortical magnification in human vision. Comprehensive evaluations across diverse datasets and multiple backbone VLMs demonstrate that LLMind consistently outperforms uniform and other bio-inspired baseline, in both *scene-level* and *region-guided* VQA settings, highlighting its utility for efficient and scalable multimodal intelligence.

Future Work: Looking forward, we aim to extend this framework toward more generative and 3D-aware vision-language tasks, including object-centric descriptions, 3D VQA, and compression-aware perception for neural rendering pipelines. We hope this work encourages further exploration of perceptually grounded representations in VLMs.

Acknowledgments: This work is supported by the MOE AcRF Tier 1: Call2/2025 under Grant No. RG160/25 and NTU Start Up Grant.

References

- [1] Abdulghani M Abdulghani, Mokhles M Abdulghani, Wilbur L Walters, and Khalid H Abed. Data augmentation with noise and blur to enhance the performance of yolo7 object detection algorithm. In *2023 Congress in Computer Science, Computer Engineering, & Applied Computing (CSCE)*, pages 180–185. IEEE, 2023. 3
- [2] Emre Akbas and Miguel P Eckstein. Object detection through search with a foveated visual system. *PLoS computational biology*, 13(10):e1005743, 2017. 3
- [3] Jean-Baptiste Alayrac, Jeff Donahue, Pauline Luc, Antoine Miech, Iain Barr, Yana Hasson, Karel Lenc, Arthur Mensch, Katherine Millican, Malcolm Reynolds, et al. Flamingo: a visual language model for few-shot learning. *Advances in neural information processing systems*, 35:23716–23736, 2022. 1
- [4] Douglas N Arnold and Jonathan P Rogness. Möbius transformations revealed. *Notices of the American Mathematical Society*, 55(10):1226–1231, 2008. 2
- [5] Shuai Bai, Keqin Chen, Xuejing Liu, Jialin Wang, Wenbin Ge, Sibao Song, Kai Dang, Peng Wang, Shijie Wang, Jun Tang, et al. Qwen2. 5-vl technical report. *arXiv preprint arXiv:2502.13923*, 2025. 1, 7
- [6] Benjamin Balas, Lisa Nakano, and Ruth Rosenholtz. A summary-statistic representation in peripheral vision explains visual crowding. *Journal of vision*, 9(12):13–13, 2009. 2
- [7] Daniel Bolya, Cheng-Yang Fu, Xiaoliang Dai, Peizhao Zhang, Christoph Feichtenhofer, and Judy Hoffman. Token merging: Your vit but faster. *arXiv preprint arXiv:2210.09461*, 2022. 2
- [8] Gianni Brauwers and Flavius Frasinca. A general survey on attention mechanisms in deep learning. *IEEE transactions on knowledge and data engineering*, 35(4):3279–3298, 2021. 2
- [9] Danny da Costa, Lukas Kornemann, Rainer Goebel, and Mario Senden. Convolutional neural networks develop major organizational principles of early visual cortex when enhanced with retinal sampling. *Scientific Reports*, 14(1):8980, 2024. 3
- [10] Wenliang Dai, Junnan Li, Dongxu Li, Anthony Tiong, Junqi Zhao, Weisheng Wang, Boyang Li, Pascale N Fung, and Steven Hoi. Instructblip: Towards general-purpose vision-language models with instruction tuning. *Advances in neural information processing systems*, 36:49250–49267, 2023. 1
- [11] PM Daniel and D Whitteridge. The representation of the visual field on the cerebral cortex in monkeys. *The Journal of physiology*, 159(2):203, 1961. 2
- [12] Arturo Deza and Talia Konkle. Emergent properties of foveated perceptual systems. *arXiv preprint arXiv:2006.07991*, 2020. 3
- [13] Keyan Ding, Kede Ma, Shiqi Wang, and Eero P Simoncelli. Image quality assessment: Unifying structure and texture similarity. *IEEE transactions on pattern analysis and machine intelligence*, 44(5):2567–2581, 2020. 4
- [14] John Duncan. Selective attention and the organization of visual information. *Journal of experimental psychology: General*, 113(4):501, 1984. 2
- [15] Jeremy Freeman and Eero P Simoncelli. Metamers of the ventral stream. *Nature neuroscience*, 14(9):1195–1201, 2011. 2
- [16] Karl Friston. The free-energy principle: a unified brain theory? *Nature reviews neuroscience*, 11(2):127–138, 2010. 2
- [17] Stephanie Fu, Mark Hamilton, Laura Brandt, Axel Feldman, Zhoutong Zhang, and William T Freeman. Featup: A model-agnostic framework for features at any resolution. *arXiv preprint arXiv:2403.10516*, 2024. 3
- [18] Zhangwei Gao, Zhe Chen, Erfei Cui, Yiming Ren, Weiyun Wang, Jinguo Zhu, Hao Tian, Shenglong Ye, Junjun He, Xizhou Zhu, et al. Mini-internvl: a flexible-transfer pocket multi-modal model with 5% parameters and 90% performance. *Visual Intelligence*, 2(1):32, 2024. 5
- [19] Andrey Gizdov, Shimon Ullman, and Daniel Harari. Variable resolution improves visual question answering under a limited pixel budget. In *European Conference on Computer Vision*, pages 289–298. Springer, 2024. 3, 7
- [20] Andrey Gizdov, Shimon Ullman, and Daniel Harari. Seeing more with less: Human-like representations in vision models. In *Proceedings of the Computer Vision and Pattern Recognition Conference*, pages 4408–4417, 2025. 3, 7
- [21] Yash Goyal, Tejas Khot, Douglas Summers-Stay, Dhruv Batra, and Devi Parikh. Making the v in vqa matter: Elevating the role of image understanding in visual question answering. In *Proceedings of the IEEE conference on computer vision and pattern recognition*, pages 6904–6913, 2017. 2
- [22] Agrim Gupta, Piotr Dollar, and Ross Girshick. Lvis: A dataset for large vocabulary instance segmentation. In *Proceedings of the IEEE/CVF conference on computer vision and pattern recognition*, pages 5356–5364, 2019. 6
- [23] Kai Han, Yunhe Wang, Hanqing Chen, Xinghao Chen, Jianyuan Guo, Zhenhua Liu, Yehui Tang, An Xiao, Chunjing Xu, Yixing Xu, et al. A survey on vision transformer. *IEEE transactions on pattern analysis and machine intelligence*, 45(1):87–110, 2022. 2
- [24] Anne Harrington, Vasha DuTell, Mark Hamilton, Ayush Tewari, Simon Stent, William T Freeman, and Ruth Rosenholtz. Coco-periph: bridging the gap between human and machine perception in the periphery. In *The Twelfth International Conference on Learning Representations*, 2023. 3
- [25] Mary Hayhoe and Dana Ballard. Eye movements in natural behavior. *Trends in cognitive sciences*, 9(4):188–194, 2005. 2
- [26] Menglin Jia, Luming Tang, Bor-Chun Chen, Claire Cardie, Serge Belongie, Bharath Hariharan, and Ser-Nam Lim. Visual prompt tuning. In *European conference on computer vision*, pages 709–727. Springer, 2022. 3
- [27] Salman Khan, Muzammal Naseer, Munawar Hayat, Syed Waqas Zamir, Fahad Shahbaz Khan, and Mubarak Shah. Transformers in vision: A survey. *ACM computing surveys (CSUR)*, 54(10s):1–41, 2022. 2
- [28] George Killick, Paul Henderson, Paul Siebert, and Gerardo Aragon-Camarasa. Foveation in the era of deep learning. *arXiv preprint arXiv:2312.01450*, 2023. 3, 7
- [29] Michael Land and Benjamin Tatler. *Looking and acting: vision and eye movements in natural behaviour*. Oxford University Press, 2009. 2

- [30] Bohao Li, Rui Wang, Guangzhi Wang, Yuying Ge, Yixiao Ge, and Ying Shan. Seed-bench: Benchmarking multimodal llms with generative comprehension. *arXiv preprint arXiv:2307.16125*, 2023. 2
- [31] Bo Li, Yuanhan Zhang, Dong Guo, Renrui Zhang, Feng Li, Hao Zhang, Kaichen Zhang, Peiyuan Zhang, Yanwei Li, Ziwei Liu, et al. Llava-onevision: Easy visual task transfer. *arXiv preprint arXiv:2408.03326*, 2024. 2, 7
- [32] Junnan Li, Dongxu Li, Silvio Savarese, and Steven Hoi. Blip-2: Bootstrapping language-image pre-training with frozen image encoders and large language models. In *International conference on machine learning*, pages 19730–19742. PMLR, 2023. 1
- [33] Haoyu Lu, Wen Liu, Bo Zhang, Bingxuan Wang, Kai Dong, Bo Liu, Jingxiang Sun, Tongzheng Ren, Zhuoshu Li, Hao Yang, et al. Deepseek-vl: towards real-world vision-language understanding. *arXiv preprint arXiv:2403.05525*, 2024. 8
- [34] Hristofor Lukanov, Peter König, and Gordon Pipa. Biologically inspired deep learning model for efficient foveal-peripheral vision. *Frontiers in Computational Neuroscience*, 15:746204, 2021. 3
- [35] Andrés Marafioti, Orr Zohar, Miquel Farré, Merve Noyan, Elie Bakouch, Pedro Cuenca, Cyril Zakka, Loubna Ben Allal, Anton Lozhkov, Nouamane Tazi, et al. Smolvlm: Redefining small and efficient multimodal models. *arXiv preprint arXiv:2504.05299*, 2025. 5, 7
- [36] Juhong Min, Yucheng Zhao, Chong Luo, and Minsu Cho. Peripheral vision transformer. *Advances in Neural Information Processing Systems*, 35:32097–32111, 2022. 3
- [37] John Olsen. The geometry of möbius transformations. *Rochester: University of Rochester*, 2010. 2
- [38] Beatriz Paula and Plinio Moreno. Learning to search for and detect objects in foveal images using deep learning. In *Iberian Conference on Pattern Recognition and Image Analysis*, pages 223–237. Springer, 2023. 3
- [39] Yongming Rao, Wenliang Zhao, Benlin Liu, Jiwen Lu, Jie Zhou, and Cho-Jui Hsieh. Dynamicvit: Efficient vision transformers with dynamic token sparsification. *Advances in neural information processing systems*, 34:13937–13949, 2021. 2
- [40] Frédérique Robert-Inacio, Rémy Scaramuzzino, Quentin Stainer, and Edith Kussener-Combier. Biologically inspired image sampling for electronic eye. In *2010 Biomedical Circuits and Systems Conference (BioCAS)*, pages 246–249. IEEE, 2010. 3, 7
- [41] Dustin Schwenk, Apoorv Khandelwal, Christopher Clark, Kenneth Marino, and Roozbeh Mottaghi. A-okvqa: A benchmark for visual question answering using world knowledge. In *European conference on computer vision*, pages 146–162. Springer, 2022. 2
- [42] Leo Schwinn, Doina Precup, Björn Eskofier, and Dario Zanca. Behind the machine’s gaze: Neural networks with biologically-inspired constraints exhibit human-like visual attention. *arXiv preprint arXiv:2204.09093*, 2022. 2
- [43] James C Spall. Multivariate stochastic approximation using a simultaneous perturbation gradient approximation. *IEEE transactions on automatic control*, 37(3):332–341, 2002. 2
- [44] Hans Strasburger, Ingo Rentschler, and Martin Jüttner. Peripheral vision and pattern recognition: A review. *Journal of vision*, 11(5):13–13, 2011. 2
- [45] Panqu Wang and Garrison W Cottrell. Central and peripheral vision for scene recognition: A neurocomputational modeling exploration. *Journal of vision*, 17(4):9–9, 2017. 3
- [46] Peng Wang, Shuai Bai, Sinan Tan, Shijie Wang, Zhihao Fan, Jinze Bai, Keqin Chen, Xuejing Liu, Jialin Wang, Wenbin Ge, et al. Qwen2-vl: Enhancing vision-language model’s perception of the world at any resolution. *arXiv preprint arXiv:2409.12191*, 2024. 1
- [47] Wenhui Wang, Furu Wei, Li Dong, Hangbo Bao, Nan Yang, and Ming Zhou. Minilm: Deep self-attention distillation for task-agnostic compression of pre-trained transformers. *Advances in neural information processing systems*, 33:5776–5788, 2020. 4
- [48] Yulin Wang, Yang Yue, Yang Yue, Huanqian Wang, Haojun Jiang, Yizeng Han, Zanlin Ni, Yifan Pu, Minglei Shi, Rui Lu, et al. Emulating human-like adaptive vision for efficient and flexible machine visual perception. *Nature Machine Intelligence*, pages 1–19, 2025. 2
- [49] Mingrui Wu, Xinyue Cai, Jiayi Ji, Jiale Li, Oucheng Huang, Gen Luo, Hao Fei, Guannan Jiang, Xiaoshuai Sun, and Rongrong Ji. Controlmlm: Training-free visual prompt learning for multimodal large language models. *Advances in Neural Information Processing Systems*, 37:45206–45234, 2024. 2, 3, 6, 7
- [50] An Yang, Anfeng Li, Baosong Yang, Beichen Zhang, Binyuan Hui, Bo Zheng, Bowen Yu, Chang Gao, Chengen Huang, Chenxu Lv, et al. Qwen3 technical report. *arXiv preprint arXiv:2505.09388*, 2025. 2, 8
- [51] Haoxuan You, Haotian Zhang, Zhe Gan, Xianzhi Du, Bowen Zhang, Zirui Wang, Liangliang Cao, Shih-Fu Chang, and Yinfei Yang. Ferret: Refer and ground anything anywhere at any granularity. *arXiv preprint arXiv:2310.07704*, 2023. 6
- [52] Lin Zhang, Ying Shen, and Hongyu Li. Vsi: A visual saliency-induced index for perceptual image quality assessment. *IEEE Transactions on Image processing*, 23(10):4270–4281, 2014. 4